Available online at www.sciencedirect.com

ScienceDirect

Procedia CIRP 128 (2024) 411–417

www.elsevier.com/locate/procedia

34th CIRP Design Conference

Innovative Autothermal Reactor Design via Additive Manufacturing: Optimization of Catalytic Exothermic Reactions Using Porous Media for Heat Management

Masoud Mahmoudizadeh[a,*], Christoph Klahn[b], Roland Dittmeyer[a]

[a]*Karlsruhe Institute of Technology (KIT), Institute for Micro Process Engineering (IMVT), 76344 Eggenstein-Leopoldshafen, Germany*
[b]*Karlsruhe Institute of Technology (KIT), Institute of Mechanical Process Engineering and Mechanics (MVM), 76131 Karlsruhe, Germany*

[*] Corresponding author. Tel.: +49-7216-082-4201. *E-mail address:* Masoud.mahmoudizadeh@kit.edu

Abstract

Designing autothermal reactors demands meticulous heat management throughout their structure. In cases where reaction heat is sourced from catalytic exothermic reactions, the distribution of this heat becomes critical. This paper explores the utilization of additive manufacturing techniques to fabricate reactors in a single, seamless process. This innovative approach allows for the precise mixing of fuel and oxidant, facilitating reactions in accordance with predefined patterns. Specifically, the study investigates the incorporation of a porous medium, acting as a diffusive medium for the oxidant (e.g. air). The reaction heat is generated at the catalyst sites when the fuel (e.g. methane) reacts with the oxidant. To benchmark this innovative design, a laser-cut distributor with air holes in series is used as a point of comparison. Employing additive manufacturing techniques, these reactors are crafted from high-temperature stainless steel Crofer 22 APU using laser-based powder bed fusion (PBF-LB/M). The solid and porous components are produced with parameters individually optimized for each part. Notably, flow uniformity, temperature profile along the reactor and concentration distribution of oxygen, derived from simulation outcomes, emerge as pivotal factors in effectively coupling exothermic and endothermic reactions within the system. It leads printing flexible and complex designs in only one step.

Keywords: Reactor Design; Additive Manufacturing; Autothermal Reactor; Gas Distribution Design; Heat Management; Porous Medium

Nomenclature

AM	Additive Manufacturing
CMC	Catalytic Methane Combustion
CPR	Catalytic Plate Reactor
MSR	Methane Steam Reforming
SR	Steam Reforming

1. Autothermal reactors

Steam reforming (SR) of hydrocarbons is recognized for providing the highest hydrogen concentration compared to alternative processes like catalytic partial oxidation and autothermal reforming [1]. However, SR is an inherently endothermic process, necessitating an efficient method for supplying heat in a reactor. Traditionally, SR is conducted in a fixed-bed catalytic reactor with a prolonged residence time [2]. Nevertheless, the fixed-bed design presents challenges such as heat transfer limitations and internal diffusion, prompting exploration into alternative reactor designs, such as the catalytic plate reactor (CPR).

The CPR design exhibits superior heat and mass transfer characteristics compared to conventional fixed-bed designs. It enables the concurrent operation of highly endothermic reactions like methane steam reforming (MSR) and exothermic reactions like catalytic methane combustion (CMC) in separate flow channels [3]. The proximity of the exothermic heat source to endothermic reaction sites significantly reduces overall heat transfer resistance [4]. Additionally, utilizing catalytic combustion for heat supply offers advantages over gas-phase combustion. Catalytic combustion occurs at lower temperatures than gas-phase combustion, mitigating NO formation. The lower operating temperature also expands the range of material choices for CPR design [5].

However, implementing catalytic combustion in a CPR introduces localized thermal gradients (hot spots), particularly near the inlets, due to the imbalance between generated and absorbed heat in combustion and reforming reaction zones [6]. Such thermal imbalances lead to issues such as material failure and catalyst delamination, arising from the differing thermal expansion coefficients of the coated catalyst and the metal plate. Large thermal gradients also diminish the catalytic active surface area, consequently affecting the conversion rate of reactants [7].

2212-8271
10.1016/j.procir.2024.04.011

Certain research has suggested the implementation of segmented catalyst layers [8,9], which, however, comes with the drawback of not fully utilizing the reactor's entire surface for the reaction. In the current investigation, an inventive design created through additive manufacturing (AM) is proposed as an alternative. This design aims to address the issue of controlling the heat profile along the length of the reactor by facilitating the mixing of air and fuel.

2. Catalytic compact combustor

Utilizing ultra-compact planar reactors, distinguished by their elevated surface-to-volume ratio, offers numerous benefits, such as a generous surface area that fosters catalytic reactions and effective heat regulation for stacked systems. In this context, a CPR for the combustion of CH_4 is examined in conjunction with a steam reformer, aimed at decentralized hydrogen production through an ultra-compact autothermal system. Consequently, this study exclusively focuses on the combustion design, evaluating two Designs, A and B, as depicted in the corresponding Figure 1. The reactor's characteristics and operating conditions for simulation are detailed in Table 1 .

Variable	Amount
Gas phase	
Inlet Composition	$0.1CH_4$/0.9Air
Temperature	693.15 K
Pressure	1 bar
Velocity	3 m s^{-1}
Geometry	
Channel Length (L)	100 mm
Channel Height (H)	0.3 mm
Number of channels	60
Hole/Porous depth of air distributor (S)	0.7 mm
Catalyst layer	
Thickness (δ)	20 μm
Porosity	0.4
Tortuosity	4
Thermal conductivity	0.4 W m^{-1} K^{-1}
Kinetics	
Pre-exponential factor (K_0)	4×10^8 s^{-1}
Activation energy (E)	90 kJ mol^{-1}
Solid wall	
Thickness (S)	0.7 mm
Thermal conductivity	25 W m^{-1} K^{-1}

Table 1. The operational parameters and distinctive features of CPR used for 2D simulation in this study.

The reactor plates are constructed using Crofer 22 (VDM Metals, Germany), with their specified dimensions outlined in Table 1. in case of Design A, these plates are precisely cut according to the design, and microchannels are formed through a chemical etching process. Subsequently, the plates are seamlessly integrated using laser welding techniques. The design of the laser seams is carefully structured to enable the scalable assembly of the reactor by increasing the number of plates.

The catalyst utilized in this study is composed of $1.5Pd-1.5Pt/Al_2O_3$ and is applied to the microchannels using a screen printing coating technique. The weight of the catalyst and the thickness of the coated catalyst layer are determined for simulation purposes.

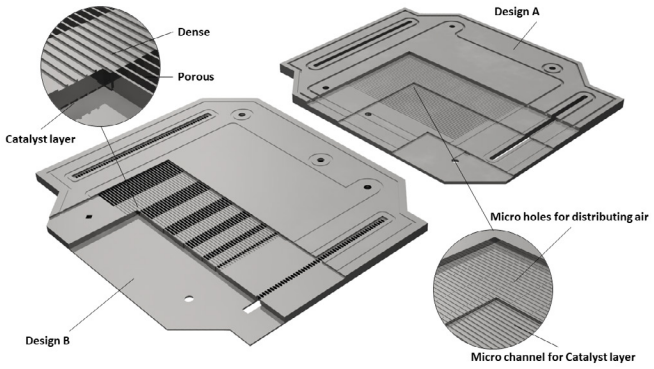

Fig. 1. An ultra-compact planar catalytic reactor composed of catalytic plates designed for CMC.

In the case of Design B, as a proof of concept derived from the simulation data, a sample is fabricated using PBF-LB/M aiming at integrating into an autothermal steam reformer for hydrogen production. Further details will be expounded upon in Section 5.

3. 2D simulation before the fabrication

A 2D non-isothermal simulation was performed to compare Design A and Design B. The primary goal of this simulation was to analyze flow distribution, uniformity, and the heat generated by the combustion reaction. Cross-sections of both designs are illustrated in Figure 2, providing visual insights into their characteristics. Mathematical formulations for this simulation can be found in Appendix.

For the catalytic combustion reaction of CH_4, the reaction rate (r) is expressed as:

$$r = K_0 \cdot \exp\left(-\frac{E}{RT}\right) \cdot C_{CH_4} \tag{1}$$

where the relevant parameters are detailed in Table 1. Here, R represents the universal gas constant (8.314 J/mol/K), T denotes the reaction temperature, and C_{CH4} signifies the concentration of the CH_4 species.

In summary, the fluid flow is modeled using weakly compressible Navier-Stokes equations in the flow channels, while the Darcy-Brinkman model is employed to capture flow in porous catalysts due to pressure gradients. Convection-diffusion equations are utilized to solve mass-fraction gradients of chemical species in the flow channels. Temperature profiles in the flow channels are determined by resolving the convection-conduction equation, and temperature distributions in porous catalysts are obtained using a pseudo-homogeneous heat-transfer model. The temperature distribution in the solid Crofer plate, serving as a heat-transfer medium between the air and fuel (CH_4) channels, is determined through the information provided by supplier [10]. Crofer is chosen for its high structural stability and a melting point of approximately 1510-1530 °C, making it an ideal substrate for coating various catalysts. Thermal conductivities, heat capacities, and viscosities of chemical components are calculated as functions of temperature. The coupled set of partial differential equations is solved

using the commercially available simulation software package COMSOL multiphyisics version 6.0, which employs the finite-element method. The CPR models are based on a automatically generated mesh, with more mesh elements employed at the catalyst inlets to capture larger variations in reaction rates and thermal gradients. All solutions are resolved using a finer mesh, and mesh-independent solutions are obtained for all runs with a convergence criterion of 1×10^{-5} absolute error.

Several assumptions are made in developing the numerical models, including the application of the ideal gas law under high-temperature and low-pressure conditions, fully-developed laminar flow in the channels, isotropic catalyst layers with all reactions occurring within these layers, and neglect of body forces.

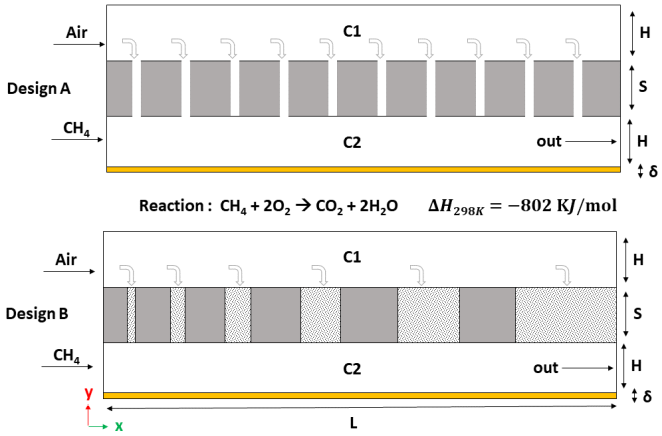

Fig. 2. A graphical representation of the simulated domains for Catalytic Plate Reactor designs A and B is presented in a two-dimensional view.

Figure 3 illustrates the temperature profile along the center line of the channel C2 (depicted in Figure 2) for designs A and B.

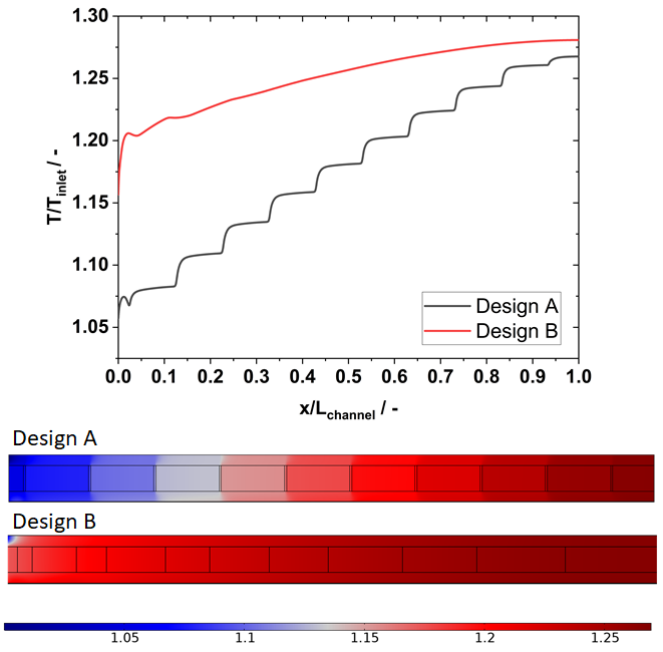

Fig. 3. Temperature profile and line graph along the bottom channel C2 for design A and B.

The rise in temperature in the initial segment of the channels indicates a swift increase, aligning with the exothermic nature of CMC. In Design B, the T/T_{inlet} ratio is approximately 1.16, while Design A shows around 1.06. This discrepancy is attributed to the higher activity in Design B, where the diffusion of gases to access active catalyst sites is facilitated at lower velocities at the beginning of the channel. At each stage, including micro holes or porous segments, the temperature elevation results from the O_2 addition of to the fuel, initiating the reaction. Notably, the final temperature at the outlet of the channel for Design B is approximately 1.28, slightly exceeding that of Design A.

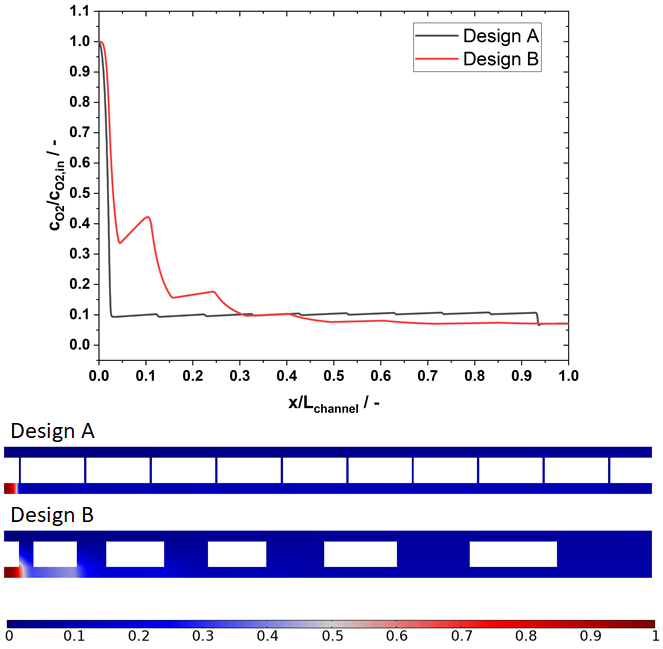

Fig. 4. The oxygen-to-inlet-oxygen ratio profiles and line graph along the bottom channel C2 for Designs A and B.

Figure 4 illustrates the O_2 profile in comparison to its inlet concentration. Notably, Design A exhibits a rapid injection, reaching approximately 90% of its initial concentration in the first hole. In another case, Design B demonstrates a gradual decrease, with 65% of its initial concentration in the first segment, followed by an additional 25% in the second porous segment. Additionally, the pressure drop along C2 restricts the passage of the oxygen stream through the middle holes for Design A. However, an exponential increase in the size of the porous segments along the reactor facilitates the penetration of O_2 into the middle segments for Design B.

Figure 5 depicts the O_2 to CH_4 ratio as a significant influencing factor. The key observation is that, for a lean condition in CMC, there is a consistent demand for excess oxygen to sustain the reaction along the reactor. Notably, in Design A, this ratio surpasses 2, while Design B maintains a value around 0.5. In lean conditions, an excess of O_2 is always expected in the system.

Specifically, Design B exhibits a ratio of O_2 to CH_4 of approximately 0.5 in the first segment, suggesting that, for this design, the Air to CH_4 ratio, which is around 10 in this study, should be considered higher. Subsequent segments in both designs demonstrate O_2 to CH_4 ratios exceeding stoichiometric ratio, reaching at the outlet to approximately 6 and slightly above 6.5 for Design A and Design B, respectively.

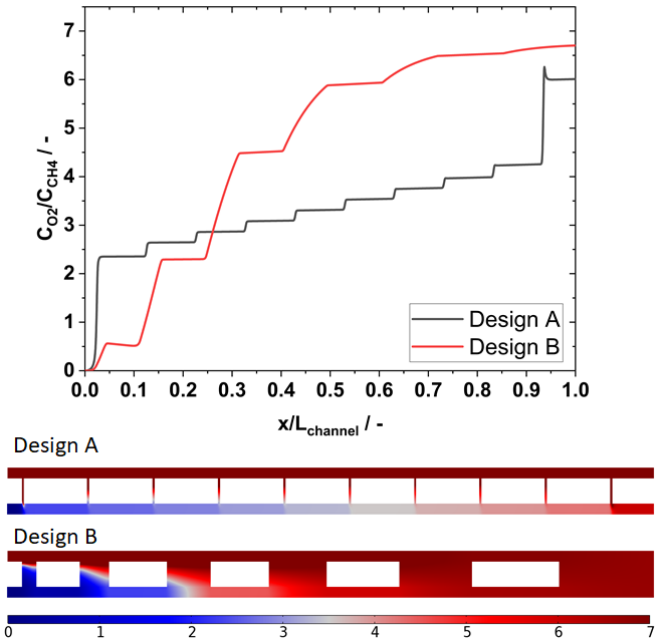

Fig. 5. The oxygen-to-methane ratio profiles and line graph along the bottom channel C2 for Designs A and B.

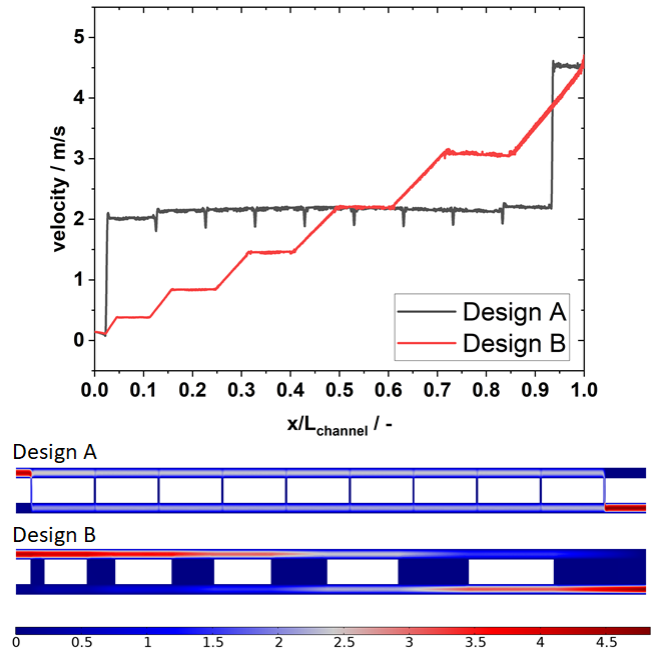

Fig. 6. The velocity magnitude profiles and line graph along the bottom channel C2 for Designs A and B.

Examining the outcomes presented in Figure 6 reveals the uniformity of velocity along channel C2. As previously noted, Design A exhibits challenges in the even distribution of O_2 within channel C2. Notably, two distinct and sharp injections are observed at the first and last holes. In contrast, Design B showcases a progressively increasing step-wise velocity profile, ranging from below 0.5 m/s to 5 m/s.

4. Discussion

The results presented suggest that adopting an oxygen feed with an exponentially decreasing profile (refer to Figure 4) contributes to achieving a uniform temperature profile. This approach can be implemented into the systems consisting of endothermic reactions, providing the requisite heat for the reaction. To implement such a temperature profile, exploring technological solutions for oxygen feed distribution becomes crucial. One potential solution involves the development of a fully automated design, followed by additive manufacturing of the reactors based on the operational conditions of the process.

Furthermore, for processes operating at elevated temperatures, utilizing a porous structure as a substrate for additional coating with an oxygen-selective layer, known as the utilization of oxygen-permeable membranes, becomes feasible. In a related context, Huppmeier et al. [11] explored the use of a pure oxygen stream on the retentate side and a staged membrane with decreasing permeability along the axis. This design enables an oxygen feed distribution that approximates the exponentially decreasing profile mentioned earlier. However, the traditional implementation of such a solution poses technological challenges, especially in assembling a membrane with variable permeance, necessitating either a gradual increase in thickness or a decrease in porosity. Therefore, additive manufacturing based on the optimized design emerges as a promising solution to overcome the mentioned challenges.

5. Additive manufacturing of catalytic combustor with controlled air distributor

Additive manufacturing of reactor housings provides users with the flexibility to tailor the geometry according to specific preferences. In the context of catalytic combustion of fuels, such as CH_4, the distribution of the oxidant (air or O_2) can be controlled within the fuel channel using porous components (gas-permeable). This aspect of additive manufacturing has been explored in our previous research, specifically in relation to metallic supports for membranes. Our earlier investigations revealed that the pore structure undergoes variations based on changes in hatch distance, laser spot size, and scan strategy. The optimized parameters derived from these studies were subsequently employed in the fabrication of dense-porous plates made of 316L through the PBF-LB/M technique [12].

Figure 7 shows the 3D-printed plate fabricated with PBF-LB/M technique according to the results of the simulation. The design can be further optimised depending of the desired application. A list of the parameter used in this print job is illustrated in Table 2.

	Hatch	Contour
Laser power P_L (W)	180	180
Scan speed v_s (mm s^{-1})	1750	750
Hatch distance h_s (μm)	80	-
Layer thickness s (μm)	50	50

Table 2. parameters used for additive manufacturing of the Design B using PBF-LB/M technique.

The reduction of pressure drop can be achieved through adjustments in printing parameters, for instance by increasing the

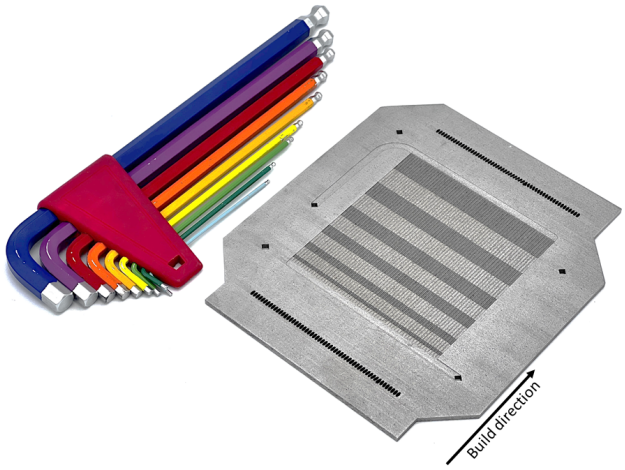

Fig. 7. Additive manufacturing of the Design B using PBF-LB/M technique.

hatch distances both the porosity and permeability increase and therefore lower pressure drop is expected [12].

6. Conclusion

Designing autothermal reactors necessitates meticulous heat management across their structure, particularly in scenarios where reaction heat stems from catalytic exothermic reactions, making heat distribution a critical aspect.This paper introduces an innovative approach that explores the utilization of additive manufacturing techniques for crafting reactors seamlessly in a single process. This technique enables precise fuel and oxidant mixing, facilitating reactions in accordance with predefined patterns. The study results showed the incorporation of a porous medium, serving as a diffusive air into CMC reactor. Based on a comprehensive 2D simulation, an exploration of various parameters for two proposed designs was conducted. The results notably indicate that Design B, crafted through additive manufacturing, exhibits a remarkable degree of tunability in terms of flow distribution. Moreover, it allows for a controlled temperature profile along the reactor, contingent upon the positioning of hot and cold spots within the system. This suggests that the additive manufacturing process not only enhances flexibility in adjusting flow patterns but also provides a level of precision in temperature control, showcasing its potential for optimized performance in practical applications.

Acknowledgements

This research was funded by the Arbeitsgemeinschaft industrieller Forschungsvereinigungen Otto von Guericke e.V. (AiF) under the agreement, ZF4591901ZG8. The authors express gratitude to Manuel Hofheinz for his assistance in the sample printing process using the SLM.

Appendix

A. *free-flow channel of combustion*

A.1. *momentum transfer and mass conservation*

momentum in x direction

$$\rho_{mix}(u_x\frac{\partial u_x}{\partial x}+u_y\frac{\partial u_x}{\partial y})=-\frac{\partial P}{\partial x}+\frac{\partial}{\partial x}(2\mu_{mix}\frac{\partial u_x}{\partial x}-\frac{2}{3}\mu_{mix}(\frac{\partial u_x}{\partial x}+\frac{\partial u_y}{\partial y}))+\frac{\partial}{\partial y}(\mu_{mix}(\frac{\partial u_x}{\partial y}+\frac{\partial u_y}{\partial x})) \tag{2}$$

momentum in y direction

$$\rho_{mix}(u_x\frac{\partial u_y}{\partial x}+u_y\frac{\partial u_y}{\partial y})=-\frac{\partial P}{\partial y}+\frac{\partial}{\partial y}(2\mu_{mix}\frac{\partial u_y}{\partial y}-\frac{2}{3}\mu_{mix}(\frac{\partial u_x}{\partial x}+\frac{\partial u_y}{\partial y}))+\frac{\partial}{\partial x}(\mu_{mix}(\frac{\partial u_x}{\partial y}+\frac{\partial u_y}{\partial x})) \tag{3}$$

continuity equation

$$\rho_{mix}(\frac{\partial u_x}{\partial x}+\frac{\partial u_y}{\partial y})+(u_x\frac{\partial \rho_{mix}}{\partial x}+u_y\frac{\partial \rho_{mix}}{\partial y})=0 \tag{4}$$

In this equation, ρ_{mix} represents the density of a gas mixture, which is estimated using the ideal-gas state equation. Meanwhile, μ_{mix} denotes the viscosity of the gas mixture, which is estimated using the Wilke method as reported by Poling et al. [13].

A.2. *heat transfer and energy conservation*

$$\rho_{mix}C_{p,mix}(u_x\frac{\partial T}{\partial x}+u_y\frac{\partial T}{\partial y})=k_{mix}(\frac{\partial^2 T}{\partial x^2}+\frac{\partial^2 T}{\partial y^2}) \tag{5}$$

In this context, $C_{p,mix}$ denotes the heat capacity of a gas mixture, which is determined by computing the weighted average heat capacity of the chemical species involved. Additionally, k_{mix} represents the thermal conductivity of the gas mixture, which is estimated utilizing the Mason and Saxena method as reported by Poling et al. [13].

A.3. mass transfer

$$\rho_{mix}((u_x\frac{\partial\omega_i}{\partial x}+u_y\frac{\partial\omega_i}{\partial y})+\omega_i(\frac{\partial u_x}{\partial x}+u_y\frac{\partial u_y}{\partial y})) = \frac{\partial}{\partial x}(\rho_{mix}\omega_k\sum_{j=1,j\neq i}^{n_g}D^F_{ji}(\frac{\partial x_j}{\partial x}+\frac{\partial x_j}{\partial y} +(\frac{x_j-\omega_j}{P})(\frac{\partial P}{\partial x}+\frac{\partial P}{\partial y})))+\frac{\partial}{\partial y}(\rho_{mix}\omega_k\sum_{j=1,j\neq i}^{n_g}D^F_{ji}(\frac{\partial x_j}{\partial x}+\frac{\partial x_j}{\partial y} +(\frac{x_j-\omega_j}{P})(\frac{\partial P}{\partial x}+\frac{\partial P}{\partial y}))) \quad (6)$$

where ω and x respectively denote the mass fraction and mole fraction of chemical species. The multicomponent Fick diffusivities, denoted as D^F_{ij}, are related to the Maxwell-Stefan diffusivities as follows [14]:

$$D^{MS}_{ij} = \frac{x_i x_j\sum_{k\neq i}D^F_{ij}(adjB_i)_{kj}}{\omega_i\omega_j\sum_{k\neq i}(adjB_i)_{kj}}; where(B_i)_{jk} = -D^F_{jk}+D^F_{ik} \quad (7)$$

In the context of multicomponent diffusion in gases at low density, the Maxwell-Stefan diffusivities D^{MS}_{ij} can be substituted with the binary diffusivities D_{ij} [14]. These binary diffusivities are estimated using the Fuller equation as reported by Poling et al. [13].

A.4. Boundary conditions

Inlet conditions as shown in Figure 2

- fully developed flow with an inlet velocity $u_x = u_{in}$
- temperature $T = T_{in}$
- mass fraction $\omega_i = \omega_{i,in}$

conditions at the outlet

- pressure $P = P_{out}$
- zero flux $\frac{\partial w_i}{\partial x} = 0; \frac{\partial T}{\partial x} = 0$

at $y = 2H + S + \delta$

- $\frac{\partial u_x}{\partial y} = 0; \frac{\partial \omega_i}{\partial y} = 0; \frac{\partial T}{\partial y} = 0$

at the interface of the catalyst layer and flow channel

- no slip $u_x = 0$
- heat flux continuity $\overrightarrow{n}.(N_{channel} - N_{catalyst}) = 0$
- zero flux $\frac{\partial \omega_i}{\partial y} = 0$

B. porous catalyst layer and 3D-printed porous part

For Design A, the porous part is limited to only the catalyst layer. However, for Design B, it includes both the catalyst layer and the 3D-printed porous parts for air. Therefore, it is assumed that the reaction takes place only in the catalyst layer domain. Consequently, in the following equations, no source term is considered for the 3D-printed part of Design B ($r = 0$).

B.1. Momentum and mass conservation

momentum in x direction

$$\frac{\mu_{mix}}{\kappa}u_x = -\frac{\partial P}{\partial x}+\frac{\partial}{\partial x}(2\frac{\mu_{mix}}{\epsilon}\frac{\partial u_x}{\partial x}-\frac{2}{3}\mu_{mix}(\frac{\partial u_x}{\partial x}+\frac{\partial u_y}{\partial y})) +\frac{\partial}{\partial y}(\frac{\mu_{mix}}{\epsilon}(\frac{\partial u_x}{\partial y}+\frac{\partial u_y}{\partial x})) \quad (8)$$

momentum in y direction

$$\frac{\mu_{mix}}{\kappa}u_y = -\frac{\partial P}{\partial y}+\frac{\partial}{\partial y}(2\frac{\mu_{mix}}{\epsilon}\frac{\partial u_y}{\partial y}-\frac{2}{3}\mu_{mix}(\frac{\partial u_x}{\partial x}+\frac{\partial u_y}{\partial y})) +\frac{\partial}{\partial x}(\frac{\mu_{mix}}{\epsilon}(\frac{\partial u_x}{\partial y}+\frac{\partial u_y}{\partial x})) \quad (9)$$

continuity equation

$$\rho_{mix}(u_x\frac{\partial u_x}{\partial x}+\frac{\partial u_y}{\partial y})+(u_x\frac{\partial\rho_{mix}}{\partial x}+u_y\frac{\partial\rho_{mix}}{\partial y}) = 0 \quad (10)$$

In this equation, κ represents the permeability of the porous media, which is calculated based on the Kozeny-Carman equation [15]. Additionally, ϵ denotes the volume void fraction (porosity) of the porous media, which is assumed to be 0.4 for the catalyst layer and 0.3 for porous Crofer part in Design B.

B.2. heat transfer and energy conservation

$$\rho_{mix}C_{p,mix}(u_x\frac{\partial T}{\partial x}+u_y\frac{\partial T}{\partial y}) = k_{eff}(\frac{\partial^2 T}{\partial x^2}+\frac{\partial^2 T}{\partial y^2})+\nu r_{com}\Delta H \quad (11)$$

In this expression, H represents the enthalpy of reaction, while k_{eff} denotes the effective thermal conductivity for a porous catalyst domain, which is computed using a volume-weighted average. The thermal conductivity of the solid catalyst ($k_{cat/crofer}$) is estimated based on alumina and is given in Table 1. Therefore, the k_{eff} is calculated as follows:

$$k_{eff} = \epsilon k_{mix}+(1-\epsilon)k_{cat/crofer} \quad (12)$$

where k_{mix} represents the gas mixture thermal conductivity and $k_{cat/crofer}$ is the porous (catalyst or Crofer) layer thermal conductivity.

B.3. mass transfer

$$\rho_{mix}((u_x\frac{\partial\omega_i}{\partial x}+u_y\frac{\partial\omega_i}{\partial y})+\omega_i(\frac{\partial u_x}{\partial x}+\frac{\partial u_y}{\partial y}))$$
$$=\frac{\partial}{\partial x}(\rho_{mix}\omega_k\sum_{j=1,j\neq i}^{N_g}D^F_{ij,eff}(\frac{\partial x_j}{\partial x}+\frac{\partial x_j}{\partial y}+(\frac{x_j-\omega_j}{P})(\frac{\partial P}{\partial x}+\frac{\partial P}{\partial y})))$$
$$+\frac{\partial}{\partial y}(\rho_{mix}\omega_k\sum_{j=1,j\neq i}^{N_g}D^F_{ij,eff}(\frac{\partial x_j}{\partial x}+\frac{\partial x_j}{\partial y}+(\frac{x_j-\omega_j}{P})(\frac{\partial P}{\partial x}+\frac{\partial P}{\partial y}))$$
$$+\nu r_{com} \tag{13}$$

for calculation of $D_{ij,eff}$ the following equation was used

$$D_{ij,eff}=D_{ji,eff}=\frac{\epsilon}{\tau}\frac{1}{2}(\frac{1}{\frac{1}{D^k_i}+\frac{1}{D_{ij}}}+\frac{1}{\frac{1}{D^k_j}+\frac{1}{D_{ji}}}) \tag{14}$$

In this equation, D^k_i and D^k_j represent the Knudsen diffusion coefficients of chemical species i and j respectively. D_{ij} and D_{ji} denote the binary diffusion coefficients of chemical species i and j. The values of tortuosity (τ) are calculated using the Bruggeman correlation [16].

B.4. boundary conditions

interface boundary between catalyst layer and gas channel

- continuity: the momentum, mass, and heat flux components normal to the boundary remain continuous across the boundary; $\overrightarrow{n}.(N_{channel}-N_{porous})=0$

C. Solid plate of Crofer 22 APU

C.1. heat transfer

$$\frac{\partial^2 T}{\partial x^2}+\frac{\partial^2 T}{\partial y^2}=0 \tag{15}$$

C.2. boundary conditions

- heat flux continuity in the interface between the gas channel and solid plate; $\overrightarrow{n}.(N_{channel}-N_{porous})=0$

References

[1] G. Kolb, Fuel processing: for fuel cells, John Wiley & Sons, 2008.

[2] J. Rostrup-Nielsen, L. Christiansen, J.-H. B. Hansen, Activity of steam reforming catalysts: role and assessment, Applied Catalysis 43 (2) (1988) 287–303.

[3] J. Hunter, G. McGuire, Method and apparatus for catalytic heat exchange, Tech. rep. (1980).

[4] G. Kolb, V. Hessel, Micro-structured reactors for gas phase reactions, Chemical Engineering Journal 98 (1-2) (2004) 1–38.

[5] M. Zanfir, A. Gavriilidis, Modelling of a catalytic plate reactor for dehydrogenation–combustion coupling, Chemical Engineering Science 56 (8) (2001) 2671–2683.

[6] F. Wang, J. Zhou, G. Wang, Transport characteristic study of methane steam reforming coupling methane catalytic combustion for hydrogen production, International Journal of Hydrogen Energy 37 (17) (2012) 13013–13021.

[7] C. H. Bartholomew, Mechanisms of catalyst deactivation, Applied Catalysis A: General 212 (1-2) (2001) 17–60.

[8] H. Wang, G. Yang, S. Li, Q. Shen, Z. Li, B. Chen, Numerical study on the effect of discrete catalytic layer arrangement on methane steam reforming performance, RSC Advances 11 (5) (2021) 2958–2967.

[9] M. Mundhwa, R. D. Parmar, C. P. Thurgood, A comparative parametric study of a catalytic plate methane reformer coated with segmented and continuous layers of combustion catalyst for hydrogen production, Journal of Power Sources 344 (2017) 85–102.

[10] VDM Metals International GmbH, VDM®Crofer 22 APU, Material Data Sheet No. 414 (2021).
URL `https://www.vdmmetals.com`

[11] J. Hüppmeier, S. Barg, M. Baune, D. Koch, G. Grathwohl, J. Thöming, Oxygen feed membranes in autothermal steam-reformers–a robust temperature control, Fuel 89 (6) (2010) 1257–1264.

[12] D. Xie, R. Dittmeyer, Correlations of laser scanning parameters and porous structure properties of permeable materials made by laser-beam powder-bed fusion, Additive Manufacturing 47 (2021) 102261.

[13] B. E. Poling, J. M. Prausnitz, J. P. O'connell, et al., The properties of gases and liquids, Vol. 5, Mcgraw-hill New York, 2001.

[14] R. Bird, W. Stewart, E. Lightfoot, Transport Phenomena, J. Wiley, 2002.

[15] J. Bear, C. Braester, On the flow of two immscible fluids in fractured porous media, in: Developments in soil science, Vol. 2, Elsevier, 1972, pp. 177–202.

[16] B. Tjaden, S. J. Cooper, D. J. Brett, D. Kramer, P. R. Shearing, On the origin and application of the bruggeman correlation for analysing transport phenomena in electrochemical systems, Current Opinion in Chemical Engineering 12 (2016) 44–51.